Incommensurate correlations in the anisotropic triangular Heisenberg lattice

Andreas Weichselbaum

Physics Department, Arnold Sommerfeld Center for Theoretical Physics, and Center for NanoScience,
Ludwig-Maximilians-Universität, DE-80333 Munich, Germany

Steven R. White

Department of Physics and Astronomy, University of California, Irvine, California 92697, USA

We study the anisotropic spin-1/2 antiferromagnetic triangular Heisenberg lattice in two dimensions, seen as a set of chains with couplings J (J') along (in-between) chains, respectively. Our focus is on the incommensurate correlation that emerges in this system in a wide parameter range due to the intrinsic frustration of the spins. We study this system with traditional density matrix renormalization group using cylindrical boundary conditions to least constrain possible incommensurate order. Despite that the limit of essentially decoupled chains $J'/J \lesssim 0.5$ is not very accessible numerically, it appears that the spin-spin correlations remain incommensurate for any finite $0 < J' < J'_c$, where $J'_c/J > 1$. The incommensurate wave vector q_J, however, approaches the commensurate value corresponding to the antiferromagnetic correlation of a single chain very rapidly with decreasing J'/J, roughly as $q_J \sim \pi - c_1 (J'/J)^n e^{-c_2 J/J'}$.

I. INTRODUCTION

The anisotropic triangular spin-1/2 Heisenberg lattice has been suggested as an effective description for several organic and anorganic compounds such as Cs_2CuCl_4[1,2] or $\kappa - (ET)_2Cu_2(CN)_3$.[3–5] These bulk systems typically consist of layered structures with weak interlayer coupling, next-nearest neighbor, and spin-orbit interactions. The experimental observation of spin-liquid-like behavior in these systems in certain parameter ranges therefore sparked renewed interest in the anisotropic triangular model system.[6] The simplest effective model is depicted schematically in Fig. 1. It is viewed as a set of chains with intrachain coupling J, which is coupled in planar triangular fashion by the interchain coupling J'. In the absence of an external magnetic field, all energies can be written in units of $J := 1$, which thus yields the single dimensionless coupling parameter $J' \equiv J'/J$, as used throughout this paper unless indicated otherwise. Extensive theoretical studies have been performed on this model system,[7–13] but the full phase diagram has remained elusive, in particular, for smaller J'. Approximate numerical studies[11] found that the magnetic order vanishes near $J' \lesssim 0.85$, with a possibly continuous transition to an essentially one-dimensional collinear phase for $J' \lesssim 0.6$ (Ref. 11) [$J' \lesssim 0.3$ (Ref. 14)]. The presence of collinear versus incommensurate order at weak chain coupling J' thus remains controversial,[8–12,14] and as such represents a major motivation for this paper.

Here, we present an extensive set of density matrix renormalization group[15] (DMRG) calculations for ladders and cylinders for this system with widths ranging from 2 to 10 lattice spacings. Recently, the use of DMRG for frustrated two-dimensional (2D) systems has proven to be very powerful: the results are highly precise and unbiased for the narrower systems, and maintain acceptable accuracy to widths of about 10 or 12 chains. Careful consideration of finite-size effects has allowed strong conclusions about the 2D ground state both in an antiferromagnetically ordered system (the isotropic triangular Heisenberg model[16]) and for a

spin liquid (the kagome Heisenberg model[17]). For a review of the techniques important for such 2D DMRG studies, see Ref. 18. Of course, each system is different, and for the anisotropic triangular Heisenberg model we study here, the incommensurate correlations and the associated finite-size effects must be dealt with carefully.

For that purpose, we chose as our primary type of cluster a cylindrical geometry, with the cylinder's axis along the J direction (cf. Fig. 1). Despite our limitation to relatively small circumferences, given the strong frustration of the chains and their decoupling for $J' \ll 1$, a width of several chains appears to give a good description of the physics of the underlying two-dimensional lattice for smaller J'. We include a careful reexamination of the zigzag chain, i.e., width-2 cylinder, which is then extended to wider systems. We do find an alternation in the properties depending on whether the width is of the form
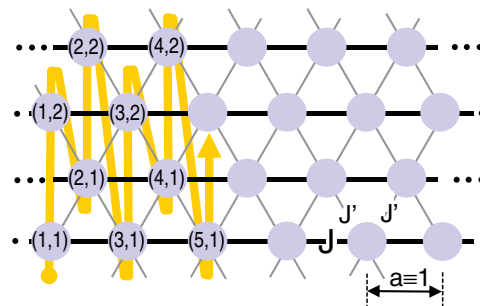

FIG. 1. (Color online) The anisotropic triangular Heisenberg lattice viewed as a set of parallel chains with intrachain coupling $J := 1$ and interchain coupling J' with lattice spacing $a := 1$. For the numerical simulation using DMRG, cylindrical boundary conditions with periodic wrapping in the transverse vertical direction are assumed unless indicated otherwise. The quasi-one-dimensional sweeping path through the triangular system used within DMRG is indicated at the left side starting with site (1,1). This path is generalized to systems of different width.

$4n$ or $4n + 2$, with n an integer, but this effect vanishes quickly with increasing n. In particular, for smaller couplings J', we find that our cylinders behave rather similarly to the zigzag chain. Overall, we see incommensurate behavior over a wide parameter range for all systems analyzed, with no indication of a collinear phase for smaller J'.[8]

This paper is thus organized as follows. Section I defines the model, and reviews its classical phase diagram. Section II describes the methods used to obtain incommensurate data, paying particular attention to boundary conditions. Section III presents the results, starting with a reexamination of the zigzag chain. This puts the stage for the analysis of increasingly wider systems, followed by summary and conclusions.

A. Anisotropic triangular Heisenberg lattice

The anisotropic triangular Heisenberg lattice is described by the Hamiltonian

$$\hat{H} = \sum_{\langle i,j \rangle} J_{ij} \hat{\mathbf{S}}_i \cdot \hat{\mathbf{S}}_j, \qquad (1)$$

with the sum over all nearest-neighbor pairs on the triangular lattice, with $J_{ij} > 0$ corresponding to frustrated antiferromagnetic (AF) nearest-neighbor interactions. Dzyaloshinskii-Moriya interactions, which we do not include, are expected to help stabilize the incommensurate phase analyzed in this paper.[8,14,19,20] The strength of these interactions may be, for example, on the order of a few percent of J for Cs_2CuCl_4.[1] The Hamiltonian in Eq. (1) is depicted schematically in Fig. 1 in terms of a width-4 system. Here, an $L \times n$ system refers to n chains of length L each. All energies are expressed in units of J, leading to the single dimensionless parameter $J' \equiv J'/J$, with explicit reference to J for emphasis only unless specified otherwise.

For practical reasons, the Hamiltonian in Eq. (1) is augmented by the additional term

$$\hat{H}_{\text{pin}} = \sum_i B_i^{\text{pin}} \hat{S}_{i,z}, \qquad (2)$$

which describes pinning of a few sites i at an open boundary. These pinning fields (i) facilitate the numerical convergence and (ii) provide a particularly convenient way, for example, to calculate and display complex correlations in a DMRG calculation. Regardless of whether one sees incommensurate correlations through correlation functions or through pinning, it is crucial that the boundary conditions alter these correlations as little as possible. In contrast, using periodic boundary conditions also along the incommensurate chain direction would be particularly troublesome, forcing commensurate locking and inducing sudden jumps in the incommensurate wave vector. Therefore, we completely avoid fully periodic boundary conditions.

B. Classical phase diagram

The classical phase diagram of the anisotropic Heisenberg lattice at zero temperature shows incommensurate order over the wide parameter range $J' \in [0,2]$ due to the system's inherent frustration. Within this parameter range, the classical ground state is given by a spiral wave with the incommensurate
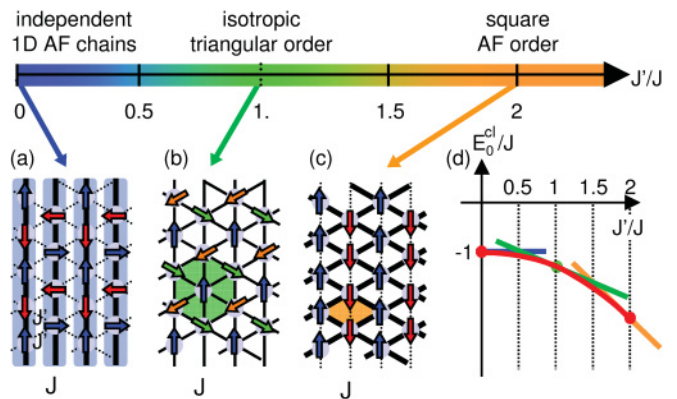

FIG. 2. (Color online) Classical phase diagram of the anisotropic triangular Heisenberg lattice at $T = 0$ demonstrating continuous incommensurate order for the entire interval $J' \in [0,2]$, having $J \equiv 1$. Specific snapshots are shown for AF correlation for $J' \to 0$ (panel a), triangular $120°$ order at the isotropic point $J' = 1$ (panel b), and square AF ordering for $J' \geqslant 2$ (panel c). Panel (d) shows the classical ground-state energy per site for the spiral wave in $J' \in [0,2]$ [red (dark gray) line]. The three straight tangential lines around the point $J' \in \{0,1,2\}$ assume the frozen spin configurations at these points, respectively. For $J' \geqslant 2$, finally, the ground-state configuration is given by the commensurate square AF order.

wave vector q_J pointing along the J direction, $\vec{q} = q_J^{cl} \hat{e}_J$.[21,22] The classical spiral wave is defined as a set of spins rotated in some arbitrary but fixed two-dimensional plane by an angle $\vec{q} \cdot \vec{r}_i$, with $\vec{r}_i$ the position of spin i within the triangular lattice. Then, for arbitrary amplitude $q \equiv q_J^{cl}$, the energy per site of the spiral wave in the J direction is given by

$$E_q^{cl}(J') = \cos(q) + 2J' \cos\left(\tfrac{q}{2}\right),$$

having assumed spins of unit length, i.e., $|S| \equiv 1$, and lattice spacing $a \equiv 1$. This energy is minimized by $\cos(\frac{q_J^{cl}}{2}) = -\frac{J'}{2}$ for $|J'| \leqslant 2$, resulting in the classical ground-state energy per site E_0^{cl} for the incommensurate spiral wave with vector vector q_J^{cl} given by

$$q_J^{cl}(J') = 2\left[\pi - \cos^{-1}\left(-\tfrac{J'}{2}\right)\right], \qquad (3)$$

$$E_0^{cl}(J') = -1 - \tfrac{1}{2}(J')^2 \qquad (4)$$

for $J' \in [0,2]$. Here, 2π was added in q_J^{cl}, so it lies within the first Brillouin zone, while assuming the branch $\cos^{-1}(x) \in [0,\pi]$. The pitch angle θ of the spiral wave,[23] defined as the angle between two spins at neighboring chains as one moves half a lattice spacing along the chains, is given by $\theta(J') = \cos^{-1}(-\frac{J'}{2}) = \pi - q_J^{cl}/2 \in [90°, 180°]$, with $q_J^{cl} \in [0,\pi]$ for $J' \in [0,2]$.

The smooth classical incommensurate phase can be seen as the continuous transition connecting the three commensurate points $J' \in \{0,1,2\}$, as depicted in Fig. 2.

(i) For small interchain coupling $J' \ll 1$, the chains are essentially decoupled leading to antiferromagnetic spin correlation along the chains (1D-AF), as indicated in Fig. 2(a). Hence, the incommensurate wave vector q_J^{cl} approaches the

end of the Brillouin zone of a single chain, i.e., $q_J^{cl} \rightarrow \pi$ [cf. Eq. (3)]. Note that, with close to AF correlation within a single chain, the interaction between chains is strongly frustrated and hence suppressed. In particular, coinciding with our definition of a spiral wave, the spins of a neighboring chain are displaced by half a lattice constant and hence rotated by $q_J^{cl}/2 = \pi/2$, i.e., 90°. The resulting $\langle S \cdot S \rangle$ interaction across the chains is thus close to zero, further emphasizing that neighboring chains essentially decouple. Therefore, in the frozen 1D-AF configuration, $E = \langle S_i S_{i+1} \rangle = -1 = \text{const}$ in units of J, as indicated by a straight line in Fig. 2(d) around $J' = 0$.

(ii) At the isotropic point $J' = 1$, the system exhibits 120° order, as depicted in Fig. 2(b). The wave vector of the spiral wave is given by $q_J^{cl} = 2\pi/3$, i.e., a period of three sites within a chain. If the order were frozen in the 120° structure, the energy per site would be $E = -\frac{1}{2}(1 + 2J')$, as indicated by a straight line in Fig. 2(d) around $J' = 1$.

(iii) For large interchain coupling $J' \gg 1$, the lattice reduces to a square lattice along the J' couplings with weak spin coupling along one diagonal of the squares (diamonds) of strength J, as indicated in Fig. 2(c). This leads to a square AF order and, consequently, ferromagnetic (FM) order of the spins along a single chain, i.e., $q_J^{cl} \rightarrow 0$. Within the frozen square AF order, the ground-state energy per site becomes $E = 1 - 2J'$, again indicated by a straight line in Fig. 2(d). This square AF order is the true classical ground-state configuration for $J' \geqslant 2$ and agrees with Eq. (4) for $J' = 2$.

From a quantum mechanical point of view, this classical picture will be altered by quantum fluctuations. Typically, one would assume that quantum fluctuations will reduce incommensurate order. In particular, while the phase boundary toward the square AF order also exists in the quantum mechanical context, one expects that the incommensurate phase terminates at a smaller value of J', as compared to the classical phase boundary of $J' = 2$. For $J' < 1$, however, the question of whether or not quantum fluctuations fully suppress the spiral wave into a collinear configuration for small enough yet finite J' has remained controversial. From our results below, we do see clearly suppressed incommensurate order, in that the quantum mechanical q_J approaches the boundary π of the Brillouin zone significantly faster as compared to the classical case. However, the incommensurate correlations do persist for finite J', suggesting that $q_J = \pi$ is reached only for $J' = 0$.

II. METHODS

We use the density matrix renormalization group[15] on a finite two-dimensional lattice with mainly cylindrical boundary conditions. We use *traditional* DMRG in that a two-dimensional strip of certain width is mapped onto a single effectively one-dimensional chain, as indicated in Fig. 1. The resulting ground state is therefore described by a matrix-product state (MPS).[24,25] This approach provides a numerically well-controlled setting, which, however, becomes numerically expensive for smaller J', and therefore prohibits a fully converged analysis for $J' \lesssim 0.5$ for widths $n > 2$. Nevertheless, we are able to make a well-controlled and largely unbiased analysis of the incommensurate correlations down to $J' \gtrsim 0.5$.

A. Cylindrical boundary conditions to study incommensurate correlations

Incommensurate behavior is affected by boundary conditions imposed on the finite system size under consideration,[26] which hence must be dealt with carefully. For this, we performed extensive initial test calculations on the anisotropic triangular lattice with a large variety of boundary conditions. For example, to allow any type of incommensurate correlations to appear and not be frustrated, we studied systems with fully open boundary conditions up to 11×13, with weak pinning of a single site in the center of the system. All such calculations strongly indicated incommensurate spiral correlations in the direction along the chains, varying with J'. They also always gave a commensurate period of two chain spacings ($\sqrt{3}a$) for transverse correlations, i.e., *ferromagnetic* correlations in next-nearest-neighbor chains.[14]

Thus, in order to study the incommensurate correlations in a *least* constrained way, we use cylindrical boundary conditions (cyl-BC) with an even circumference, i.e., composed of an even number of chains (note that this is also compatible with the square AF order of the system for large J'). Furthermore, the very left boundary of the open chains was pinned by a small external (staggered) magnetic field, while the right boundary was *softened* by damping the Heisenberg couplings smoothly toward zero (*smooth boundary condition*).[27] The resulting combined set of boundary conditions will be referred to as cylindrical pinned with smoothing boundary condition (cps-BC). The pinning fields at the left boundary induce an (exponentially) decaying magnetization in the bulk of the system. The resulting incommensurate correlations are analyzed away from the open boundaries in the central area of the system.
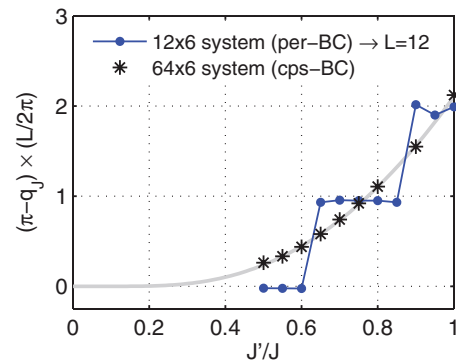

FIG. 3. (Color online) Comparison of the incommensurate wave vector $\tilde{q}_J \equiv \pi - q_J$ obtained from DMRG between a small 12×6 system with fully periodic BC (per-BC) (solid line with round symbols) and a larger 64×6 system using cps-BC [data (black asterisks) with a fit of the type $a(J')^2 e^{-b/J'}$ (gray line) taken from Fig. 8 below]. The incommensurate data for the fully periodic system was extracted from the residual $\langle S_{z,x} \rangle \sim 10^{-3}$ data derived from the calculated DMRG ground state for $S_z^{\text{tot}} = 0$, consistent with explicit $\langle S_0 \cdot S_i \rangle$ correlation data. In the fully periodic system, no pinning or smoothing was applied to guarantee full translational invariance. Due to the presence of long-range interactions, in the per-BC case, up to $m = 5000$ states had to be kept.
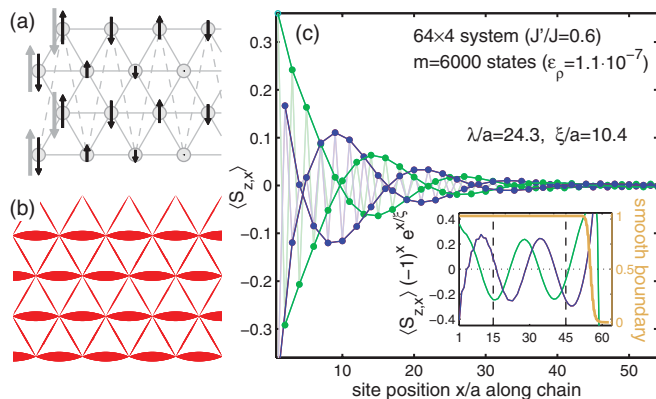
FIG. 4. (Color online) Analysis of the incommensurate correlations for 64×4 system at $J' = 0.6$ using cps-BC. Panel (a) shows the magnetization $\langle S_{z,x} \rangle$ at the open left boundary (black arrows on top of each site), as triggered by the staggered pinning fields $B_{x,y}^{\text{pin}}$ at the leftmost sites (gray arrows) with $|B| = 0.5$. The triangular lattice with sites and bonds is indicated in the background, with the bonds due the periodic BC in the vertical direction indicated by dashed lines. Panel (b) shows $\langle S \cdot S \rangle$ correlations between nearest-neighbor sites around the center of the system. These correlations are well converged, uniform, and antiferromagnetic (indicated by the same red color), with intrachain correlations $\langle S \cdot S \rangle_J \simeq -0.394$ and significantly weaker interchain correlations $\langle S \cdot S \rangle_{J'} \simeq -0.061$. Panel (c) analyzes the full $\langle S_{z,x} \rangle$ response of the system, as partly already indicated in panel (a), as a function of horizontal position for all chains. It shows the bare $\langle S_{z,x} \rangle$ data (light colors), together with the exponentially decaying oscillating envelopes (strong colors), from which the exponential decay ξ and the incommensurate period λ is determined from a phase analysis, as described in Eq. (5) and the following discussion. The inset shows the reduced purely oscillating part of $\langle S_{z,x} \rangle$. The right axis set of the inset and its corresponding data (matching colors) indicate the weights applied to the couplings for smoothing the open right boundary.
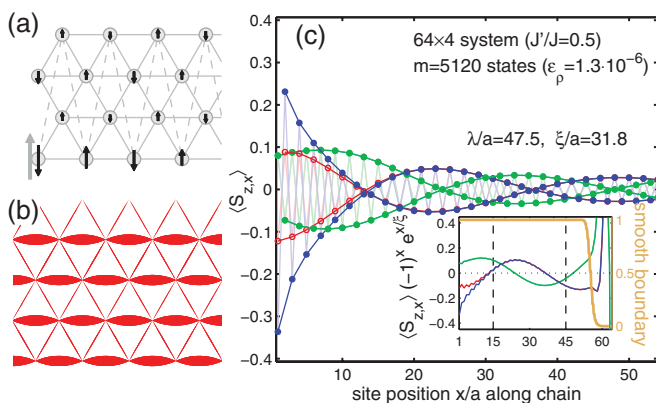

FIG. 5. (Color online) Analysis of the incommensurate correlation for the same system as in Fig. 4, except for smaller $J' = 0.5$ and the pinning field, which is applied to a *single* site at the left boundary only [indicated by the light gray arrow in panel (a); $B = 0.5$]. Panel (b) shows the intrachain correlations at the center of the system, having $\langle S \cdot S \rangle_J \simeq -0.419$ with strongly weakened interchain correlations $\langle S \cdot S \rangle_{J'} \simeq -0.038$ due to frustration. Note that $\langle S \cdot S \rangle_J$ is already close to the lower bound for the mean of $\langle S \cdot S \rangle_J \geqslant \frac{1}{4} - \ln(2) = -0.4431$, derived from the ground-state energy E_0/J of a single Heisenberg chain (Ref. 28).

1. Finite-size artifacts for small systems

Incommensurate correlations for $J' \lesssim 0.5$ exhibit (exponentially) long wavelengths $\lambda \equiv 2\pi/(\pi - q_J)$. These correlations are strongly affected by small system sizes and the boundary conditions applied, and as such may potentially be misinterpreted. An example is given in Fig. 3. For fully periodic boundary conditions (per-BC), the relatively small 12×6 system clearly shows finite-size effects of the type $\tilde{q}_J \equiv \pi - q_J \simeq \frac{2\pi}{L} n$, with $n = 0, 1, 2, \ldots$ an integer. The small and noisy deviations from pure integer n may already be considered an indicator that the system tries to break away from the periodicity enforced by given system length $L = 12$. In contrast, the incommensurate data for the larger 64×6 system, using cps-BC clearly interpolates the per-BC data in a smooth fashion. A fit of the form $\tilde{q}_J(J') = a(J')^2 e^{-b/J'}$ is included in Fig. 3 in solid gray (see also Fig. 8 later). For the fully periodic system, even for relatively large systems, the transition between uniform collinear behavior ($n = 0$) and the first "transition" to $n = 1$ will always occur at relatively large $J' \gtrsim 0.5$, which may thus be misinterpreted as a transition into a collinear phase. Note that this "transition" changes the parity or reflection symmetry of the ground state, which has been used as an argument in favor of a (possibly continuous) phase transition in the literature.[9,11]

In contrast, for all of our data using cps-BC for as small as $J' \simeq 0.3 \ldots 0.5$ for the width-4 system (not presented), we still see incommensurate behavior,[8] in that the magnetization data shows a clear onset of oscillatory behavior consistent with our fit to q_J. It has significantly larger error bars, however, since (i) many more states would actually have to be kept for full convergence given that the entanglement block entropy grows strongly for smaller J', and (ii) the corresponding wavelength $\lambda = 2\pi/(\pi - q_J)$ can no longer be determined reliably as it clearly exceeds accessible system sizes.

B. Determination of the incommensurate wave vector

The incommensurate wave vector is determined by the analysis of the system's response to the pinning fields at the left boundary using cps-BC. The procedure is illustrated for a 64×4 system for $J' = 0.6$ in Fig. 4, and with altered pinning for $J' = 0.5$ in Fig. 5. Note that despite $J' \simeq 0.6$ was suggested as the phase boundary toward collinear order,[11] both systems, Fig. 4 as well as Fig. 5, clearly show pronounced incommensurate oscillations still, while having $J' \leqslant 0.6$.

Using cps-BC, in Fig. 4(a) the leftmost site of each chain is pinned through a staggered external magnetic field $|B_{\text{pin}}| = 0.5$, which thus respects the underlying AF correlations of the Heisenberg model for smaller J'. However, the exact details of the applied pinning usually did not matter (see Fig. 5 later). After a relatively short transient region, the magnetization of each chain followed a clear exponential decay with superimposed oscillations, as seen in Fig. 4(c). The period of these oscillations usually neither is a simple multiple of the underlying lattice spacing a nor does a multiple of the period fit into the specific finite system size under investigation, i.e., the period is incommensurate. The *smoothing*[27] of the right open boundary roughly affected the right 20% of the system [see data associated with right axis in inset to Fig. 4(c)]. Within the smoothing region at the right boundary, both couplings, J as

well as J', were damped uniformly as a function of horizontal chain position x by weights that smoothly turned into an exponential decay $\propto e^{-\Lambda x}$, i.e., decreasing the couplings by a factor of $\Lambda = 2$ within one horizontal lattice spacing a. This setting has been used for smooth boundary throughout. The purpose of this smooth boundary in the cps-BC setup was tailored to blur the finite size in the direction of the chains, and hence to least constrain incommensurate correlations.

The incommensurate correlations for smaller J' then are dominated by AF correlations, as the wave vector q_J rapidly approaches the boundary of the Brillouin zone of a single chain, $q_J \to \pi$. This is seen in the zigzag structure of the bare $\langle S_{z,x} \rangle$ data for $J' = 0.6$ in Fig. 4(c) (light colors in the background), while the envelope for every other site (lines in strong color) are plain decaying oscillating $\pm \sin(\dots)$ and $\pm \cos(\dots)$ curves for even and odd chains, respectively. Note that the data for all even or odd chains in Fig. 4(c) coincides, and hence lies indistinguishable on top of each other.

The spiral correlations are analyzed then as follows. With a two-chain periodicity normal to the chains, the system can be regarded as an interleaved set of even chains (chains $2, 4, \dots$) and odd chains (chains $1, 3, \dots$). Consequently, the position x of the sites in chain direction in the odd chains ($x = \frac{1}{2}, \frac{3}{2}, \dots$, in units of lattice spacings a) is shifted by half a lattice constant with respect to the even chains ($x = 1, 2, \dots$). With $\langle S_{z,x} \rangle$ the measured spin projections in the z-direction of the spin at site position x, the exponentially decaying envelope $\langle S_{z,0} \rangle e^{-x/\xi}$ allows us to determine the correlation length ξ by fitting. With $\tilde{q}_J \equiv \pi - q_J \ll 1$ quickly becoming small for $J' < 1$, the pure oscillatory part of the spiral correlations along the chains can be extracted. Up to an irrelevant overall phase, it is given by

$$
\begin{aligned}
\langle S_{z,x} \rangle (\langle S_{z,0} \rangle e^{-x/\xi}) &\sim \cos\left[(\pi - \tilde{q}_J)x\right] \\
&= \cos(\pi x)\cos(\tilde{q}_J x) + \sin(\pi x)\sin(\tilde{q}_J x) \\
&= \begin{cases} (-1)^x \cos(\tilde{q}_J x) & \text{for } x = 1, 2, \dots \text{ (even chains)}, \\ (-1)^{\tilde{x}} \sin(\tilde{q}_J x) & \text{for } x = \frac{1}{2}, \frac{3}{2}, \dots \text{ (odd chains)}, \end{cases}
\end{aligned}
\tag{5}
$$

with $\tilde{x} \equiv x - \frac{1}{2}$ in the last line. This zigzag due to the signs together with the oscillatory envelope of sine and cosine waves is clearly seen in the main panel of Fig. 4(c). Here, the global phase is fixed through the pinning at the left boundary, thus facilitating the overall numerical convergence within the DMRG calculation. By applying staggered signs and correcting for the overall exponential decay, pure cosine (even chains) and sine waves (odd chains) can be extracted, as shown in the inset to Fig. 4(c). Here, the sign factor for odd chains needs to be understood as $(-1)^{\tilde{x}}$, as introduced with Eq. (5). The incommensurate wavelength $\lambda \equiv 2\pi/(\pi - q_J)$ of the slowly oscillating envelope can then be determined, for example, from the zero transitions of these oscillations, assuming that several periods fit into the system.

Alternatively, a phase analysis of the the cosine-sine relationship in Eq. (5) can be employed to determine q_J. For this, note that away from the open boundaries, the slow oscillations of the envelope in Fig. 4(c) or its inset are well described by $c(x) \equiv r(x)\cos(\varphi(x))$ and $s(x) \equiv r(x)\sin(\varphi(x))$, with $\varphi(x) \equiv q_J x$, up to an irrelevant overall phase, and a common decaying envelope function $r(x)$. Here, even and odd chains are only distinguished by their respective discrete sets

of values for x. Nevertheless, for example, by interpolating the sine data for odd chains halfway in-between two neighboring sites, values $(c(x), s(x))$ for a matching position x are obtained. With $\tan(\varphi(x)) = s(x)/c(x)$, the wave vector q_J can thus be determined from the slope of the calculated phase $\varphi(x)$. The amplitude $r(x)$ drops out, hence its precise value and functional dependence are unimportant. This phase analysis, indeed, represented a reliable alternative procedure to determine q_J for smaller J'. In particular, it also showed the quality of the underlying sine and cosine data, which for the systems in Figs. 4 or 5 demonstrated an excellent linear dependence of $\varphi(x)$ over the fitting range x indicated by the vertical dashed lines in the inset to Figs. 4(c) and 5(c). The specific resulting values for the exponential decay ξ and the wave vector q_J are specified with the panel.

The analysis in Fig. 4 has been repeated for exactly the same system, yet for smaller $J' = 0.5$ and with the pinning reduced to a *single* site (ssp) at the left boundary, as indicated in Fig. 5(a). If the same $J' = 0.6$ as in Fig. 4 had been taken, the altered pinning of Fig. 5 solely resulted in a modified transient behavior right next to the pinning fields at the left boundary, which also leads to a different irrelevant phase of the oscillatory part in $\langle S_{z,x} \rangle$. The resulting correlation length ξ as well as the incommensurate wave vector λ, however, are exactly the same as already indicated in Fig. 4(c), with relative differences on the order of 1%. This insensitivity of the incommensurate behavior to the exact details of the pinning at the left boundary is seen also for a wider range of J', as will be demonstrated in Fig. 7.

The analysis in Fig. 5 then is based on a system with the smaller interchain coupling $J' = 0.5$ instead. The pinning occurs on a single site at the lowest chain, considered chain #1, and hence an odd chain. Similar to Fig. 4, in the main panel Fig. 5(c), a transient behavior at the left boundary is clearly visible. Not surprisingly, the data within the odd chains differs for $x/a \lesssim 15$, given that one of them is pinned. Overall, however, data for even or odd chains quickly coincides away from the left boundary, consistent with what has already been seen in Fig. 4. Also, the data for even chains coincides from the very beginning. This is attributed to the very weak $\langle S \cdot S \rangle_{J'}$ correlation in-between the chains [see Fig. 5(b)] due to the system's inherent frustration despite the sizable J' of 0.5.

III. RESULTS

A. Review of width-2 system (zigzag chain)

The triangular system consisting of two chains is also referred to as zigzag or J_1-J_2 chain, with nearest-neighbor interaction $J_1 \equiv J'$ and next-nearest-neighbor interaction $J_2 \equiv J$. While it has been widely studied in the literature,[27,29] we carefully reexamine the zigzag chain in the entire parameter range from small to large J', with the main focus on incommensurate behavior[23] for $J' < 1$. This analysis for the width-2 system then sets the stage for the wider systems further below, which will proceed in a completely analogous fashion.

The results for the 128×2 system are summarized in Fig. 6 using cps-BC. Since for the zigzag chain the periodic boundary in the width of the system is equivalent to taking $J' \to 2J'$
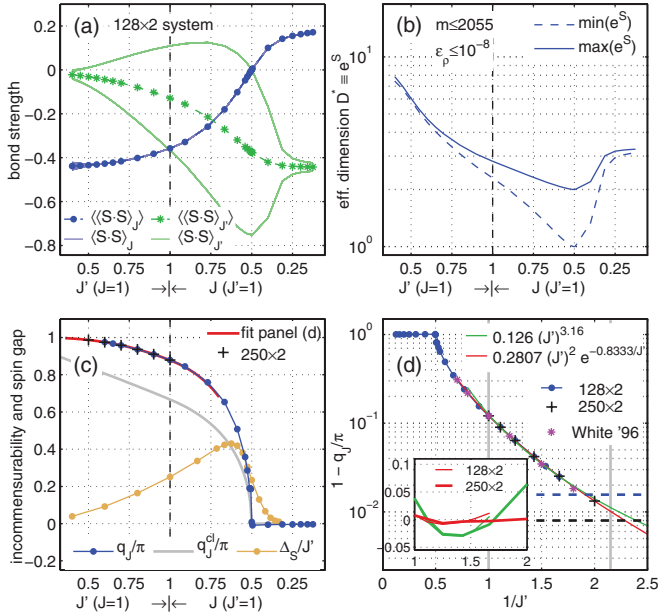
FIG. 6. (Color online) Analysis of 128×2 system (zigzag chain) around the system center using cps-BC over a wide range of J'. In panels (a)–(c), the horizontal axis shows J' for $J' < 1$, smoothly switching to the inverse $1/J'$ for $J' > 1$ [cf. Eq. (6)]. Panel (a) shows the nearest-neighbor spin correlations of individual bonds along the chains $[\langle S \cdot S \rangle_J]$ and in-between the chains $[\langle S \cdot S \rangle_{J'}]$. Here, up to dimerization, this leads to many lines lying on top of each other, with minor deviations seen for the smallest J' only. $\langle \langle S \cdot S \rangle_J \rangle$ and $\langle \langle S \cdot S \rangle_{J'} \rangle$ correspond to the averaged $\langle S \cdot S \rangle_J$ and $\langle S \cdot S \rangle_{J'}$ data, and are shown in strong colors (dashed with bullets and asterisks, respectively). Panel (b) indicates the numerical cost of the calculations in terms of the effective dimension $D^* \equiv e^S$ (see text). D^* is calculated w.r.t. to bonds of the linearized system (cf. path shown in Fig. 1). Given intrinsic even-odd alternations, for simplicity, only the maximum and minimum D^* from block decompositions w.r.t. the system center is shown. Panel (c) shows the incommensurate wave vector q_J (solid blue with bullets for 128×2 system, black pluses for larger 250×2 system), where the thick solid line for smaller J' replicates the exponential fit from panel (d). For reference, also the classical incommensurate wave vector q_J^{cl} as well as the spin gap Δ_S/J is shown, with the latter calculated for plain cylindrical BC (see text). Panel (d) analyzes the incommensurate data q_J for small J' relative to the zone boundary vs. plain inverse J' on a semilogarithmic plot. A smooth exponential fit [solid red (dark gray)], and for comparison, a plain polynomial fit [solid green (light gray)] are shown. Data for a larger 250×2 system as well as data from White '96 (Ref. 23) is included. The horizontal dashed lines indicate $2/L$, i.e., the smallest $\tilde{q}_J/\pi \equiv 1 - q_J/\pi$ reachable for given system size (color match with data in panel). The inset shows the relative deviation of both fits from the data. Thin (thick) lines are for the smaller (larger) system, while red (dark gray) [green (light gray)] lines refer to the exponential (simple polynomial) fit, respectively.

and using open BC, the boundaries are considered open in this case, while nevertheless applying pinning and smoothing as usual. The data shown in Fig. 6 covers a wide range of J' from large $J' \gg 1$ down to smaller $J' \gtrsim 0.5$. For this purpose, Figs. 6(a)–6(c) plot the data vs. J' in units of J for $J' \leqslant 1$, while for $J' > 1$, the data is plotted vs. J in units of J' in

reverse order. To be specific, while J and J' are indicated on the horizontal axis in Figs. 6(a)–6(c) for readability, what is actually plotted on the horizontal axis is

$$\zeta \equiv \begin{cases} \frac{J'}{J} & \text{for } J'/J \leqslant 1 \to \zeta \in [0,1], \\ 2 - \frac{J}{J'} & \text{for } J'/J \geqslant 1 \to \zeta \in [1,2]. \end{cases} \tag{6}$$

Overall then, $\zeta \in [0,2]$ covers the entire range $J' \in [0,\infty]$, with $\zeta = 1$ being the isotropic triangular lattice. Note that the derivative of $\zeta(J')$ is smooth across $J' = 1$, which is also reflected in the smoothness of all data across $J' = 1$ in Figs. 6(a)–6(c).

Figure 6(a) analyzes the nearest-neighbor correlations $\langle S \cdot S \rangle_J$ and $\langle S \cdot S \rangle_{J'}$ at the center of the system along and in-between the chains, respectively. The overall averages $\langle \langle S \cdot S \rangle_J \rangle$ and $\langle \langle S \cdot S \rangle_{J'} \rangle$ are shown in strong solid colors with symbols. The data for individual bonds $\langle S \cdot S \rangle_J$ and $\langle S \cdot S \rangle_{J'}$ with respect to $n_s^c = 8$ sites from both chains is shown in light colors (solid lines). Much of the data of individual bonds lies indistinguishable on top of each other, which demonstrates the uniformity of the system (larger deviations will be seen later for wider systems for small J' due to numerical issues e.g., see Fig. 8). In Fig. 6, tiny deviations in the individual bond data are seen only for the very smallest $J' = 0.4$ analyzed. Despite numerical issues as discussed with Fig. 6(b) below, this is also attributed to finite-size effects, in that the incommensurate wavelength $\lambda \equiv 2\pi/(\pi - q_J)$ reaches and rapidly extends beyond given system size for small J'.

While the $\langle S \cdot S \rangle_J$ data widely agrees with its average, the $\langle S \cdot S \rangle_{J'}$ data shows a symmetry-broken state. The interchain bonds combine two different diagonal directions, and as such shows dimerization over a wide range,[23] seen as the opening of a *dimerization bubble* in the $\langle S \cdot S \rangle_J$ data. This bubble closes, i.e., approaches its average (asterisks) for $J' \to 0$ and for large J' at $1/J' \simeq 0.241\,167$.[29] The dimerization results from spontaneous symmetry breaking along the direction of the chains with alternating weak and strong interchain bonds (interestingly, a similar symmetry breaking is encountered again later in an increasingly weaker form for the wider width-6 and width-10 systems). The width-2 system analyzed here becomes completely dimerized at the Majumdar-Ghosh point[30] $J' = 2$, as seen in Fig. 6(a) at $J/J' = 0.5$. There, both the $\langle S \cdot S \rangle_J$ data [blue (dark gray) line with bullets] as well as the upper branch in the $\langle S \cdot S \rangle_{J'}$ data [solid light green (gray) lines], pass through zero, while the lower branch in the $\langle S \cdot S \rangle_{J'}$ data reaches its strongest negative value of -0.75 due to pairwise singlet formation.

The numerical cost of a DMRG calculation is directly reflected in the effective dimension $D^* \equiv e^S$, which is plotted in Fig. 6(b). Here, S is the block entropy around the center of the system, i.e., the von Neumann entropy after tracing out approximately half of the system. Up to a prefactor, the effective dimension D^* directly indicates the dimension D of the underlying matrix product state that is required for some fixed prespecified accuracy. As such, D^* indicates the numerical cost, which in the case of DMRG scales as $\mathcal{O}(D^3)$. For reference, Fig. 6(b) also indicates the actual number of states ($m \leqslant 2055$, largest for small J') as well as the maximum discarded weight ϵ_ρ. D^* typically shows even-odd behavior and also variations depending on the explicit block partitioning

of the system. Hence, the maximum and minimum D^* across the system center is shown. As seen in Fig. 6(b), D^* saturates for large J', and exhibits a minimum at the Majumdar-Ghosh point $J' = 2$. There, D^* alternates between the minimum of 1 (at the boundary in-between two singlets) and the maximum of 2 (cutting across one singlet). Starting from the Majumdar-Ghosh point, when decreasing J', D^* increases exponentially, with a further strong boost for $J' \lesssim 0.6$ [note that Fig. 6(b) is a semilogarithmic plot]. The strong increase in numerical cost for small J' is clearly due to the effective decoupling of the chains in this parameter regime. This leads to largely independent Hilbert spaces that need to be combined in a tensor product. Nevertheless, the presence of the frustrating neighboring chains does affect the detailed nature of the effective low-energy Hilbert spaces, hence, the sweeping path across the chains as depicted in Fig. 1 is important and can not simply be replaced, for example, by a sweep preferentially along entire chains first.

The results for the incommensurate wave vector q_J are shown in Fig. 6(c) [blue (dark gray) bullets], together with data from a larger 250×2 system (black pluses) and an exponential fit for small J', replicated from Fig. 6(d) [thick red (black) line]. The incommensurate wave vector q_J vanishes at the Majumdar-Ghosh point, being zero for $J' \geqslant 2$. This phase boundary incidentally agrees with the classical incommensurability q_J^{cl} for the infinite system. On the other hand, while for small J' the classical q_J^{cl} approaches the boundary of the Brillouin zone in a linear fashion [also plotted in Fig. 6(c) for comparison], the quantum mechanical incommensurability is strongly reduced, in that q_J approaches the zone boundary of π much faster, and at first sight, even appears to vanish already for $J' \simeq 0.5$. But, as we will argue in the following, it does not.

The spin gap Δ_S of the zigzag chain [also calculated and shown in Fig. 6(c), for reference; see later discussion] is described for small J' by $\Delta_S \simeq c_1 e^{-c_2/J'}$,[23] with constants c_1 and c_2 of order one. For large J', on the other hand, the dimerization [Fig. 6(a)] as well as the spin gap [Fig. 6(c)] are expected to vanish for $1/J' = 0.241\,167$.[29] Motivated by this inverse exponential behavior of the spin gap for small J', Fig. 6(d) shows the q_J data of Fig. 6(c) vs. plain inverse J'. Moreover, in order to zoom into the boundary of the Brillouin zone, the incommensurate data q_J is plotted in terms of $\tilde{q}_J \equiv \pi - q_J$ on a semilogarithmic scale in the y direction. Clearly, the incommensurate $\tilde{q}_J$ decays fast for large x values (i.e., small J' values), close to exponentially, indeed, but by no means does $\tilde{q}_J$ show any tendency to vanish for finite J'. On the contrary, the data shows a slight upward curvature.

We fitted the data for $\tilde{q}_J$ in the interval indicated by the two vertical lines in Fig. 6(d) in two ways: (i) an exponential fit of the type

$$\tilde{q}_J\left(\tfrac{1}{J'}\right) \equiv \pi - q_J\left(\tfrac{1}{J'}\right) \cong c_1(J')^{c_3} e^{-c_2/J'}, \qquad (7)$$

and (ii) for comparison, also a plain polynomial fit. The exponential fit indicated an exponent $c_3 \simeq 2$, so c_3 was fixed to this value for the zigzag chain. The remaining fit parameters are shown in the legend of Fig. 6(d). For comparison, the plain power-law fit results in $(J')^{3.16}$, in agreement with the $\mathcal{O}(J'^3)$ estimate by Ref. 14 in the case where spiral order is selected by

fluctuations at $\mathcal{O}(J'^2)$. It is hard to discern in Fig. 6(d) which of the two fits is closer to the data, so the *relative* difference of the actual data to the fitted values is shown in an inset to Fig. 6(d). The slight positive curvature of the power-law fit in this figure appears somewhat too strong, which is clearly magnified still in the inset. In comparison, the exponential fit lies significantly closer to the actual data, which due to the large number of states kept in the calculation is well converged.

From this, we conclude that the exponential fit of the type $c_1(J')^2 e^{-c_2/J'}$, which is nonanalytic in J', fits best for the incommensurate wave vector of the zigzag chain. Moreover, from the systematic behavior seen in the incommensurability down to $J' \gtrsim 0.5$, we take this as a strong indication that $\pi - q_J$ *remains* finite for any finite $J' < 0.5$. From further calculations for $J' \sim 0.3 \ldots 0.5$ (not shown), we do see that the oscillatory bending of the S_z data as in Fig. 4 continues. The system, however, can no longer be taken large enough to accommodate even a single full period of an incommensurable wave, which would allow a reliable determination of q_J. Clearly, given the exponentially rapid decay of $\pi - q_J$ as in $e^{-c_2/J'}$, the required system sizes to actually analyze incommensurable order for small J' becomes exponentially large. With the fit parameters in Fig. 6(d), for example, the required system length estimated by $\lambda \equiv 2\pi/\tilde{q}_J$ for $J' = 0.3$ is around $\lambda \simeq 1300$ sites, while for $J' = 0.2$ it would have already grown to $\lambda \simeq 11\,500$ sites!

B. Width-4 to width-10 systems

The same analysis as for the width-2 system in Fig. 6 is performed for systems of width-4 (Fig. 7), width-6 (Fig. 8), width-8 (Fig. 10), and width-10 (Fig. 11). All systems analyzed exhibit smoothly changing incommensurate behavior for finite $J' < J'_c$, having $J'_c \gtrsim 1.25$. The width-4 system in Fig. 7 includes reference data [black pluses in Figs. 7(c) and 7(d)], with the pinning altered from an AF-pinning at the left boundary (cf. Fig. 4) to pinning of a *single* site (cf. Fig. 5). The data is clearly consistent with each other, which emphasizes the insensitivity to the exact details of the pinning at the open boundary and supports a clear two-chain periodicity normal to the chain direction in the center of the system.

For comparison, also the spin gap Δ_S was calculated for the systems up to width-8 with rudimentary finite-size scaling only.[31] The spin gap Δ_S was obtained by calculating the ground-state energy E_0^S for increasing total spin S of a system with plain cylindrical boundary conditions, i.e., in the absence of pinning fields or smoothing of the boundary. In avoiding fully periodic boundary conditions for numerical but also physical reasons (i.e., accounting for incommensurate behavior), the open boundary at the end of the cylinder can carry spinful edge excitations.[31] Since these edge states quickly decouple with increasing system length, they can and do lie within the spin gap for the width-4, -6, and -8,...systems. Thus, the total spin S was increased until a true bulk excitation was observed in the data, i.e., the measured $\langle S_{z,x} \rangle$ data was no longer exponentially confined to the boundary. The energy of this state relative to the global ground state was used to estimate the spin gap Δ_S.[31]
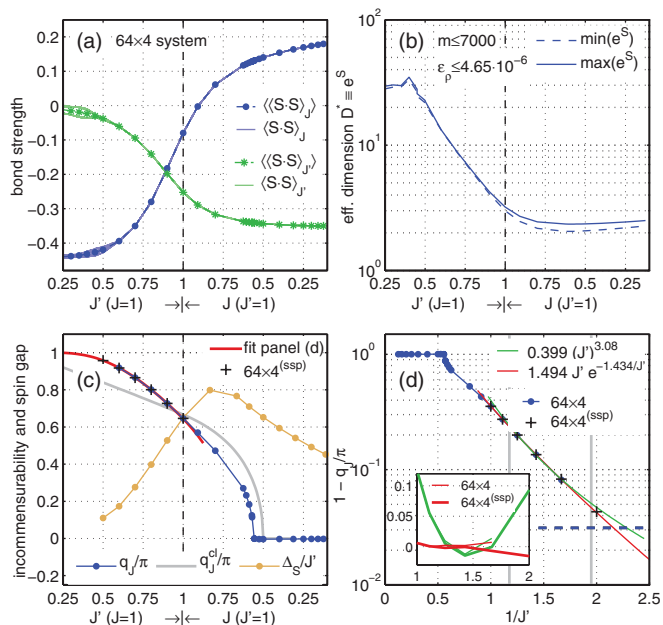
FIG. 7. (Color online) Analysis of 64×4 system using cps-BC (analysis is similar to Fig. 6; for a detailed description of panels and insets see caption there). The system shows no dimerization, with the incommensurate phase boundary at $J'_c \simeq 1.78$. Small finite-size and numerical limitations are seen for $J' < 0.5$ in (a) and (b). The exponential fit in panel (d) as in Eq. (7) gives $c_3 \simeq 1$ to a good approximation, hence, c_3 has been fixed to 1. The reference data (black crosses) shown in panels (c) and (d) derives from exactly the same physical system, with the only difference of having a single site pinned only (cf. Fig. 5).

1. Intermediate chain coupling

The major striking effect seen in the wider systems is the symmetry-broken alternation of the nearest-neighbor exchange correlation (to be referred to as dimerization) for intermediate J', as seen in Figs. 6–11. The dimerization bubble in the $\langle S \cdot S \rangle_{J'}$ data, which is strongly visible for width-2 [Fig. 6(a)], *disappears* for width-4 [Fig. 7(a)] and width-8 [Fig. 10(a)], while it clearly reappears in ever weaker form for width-6 [Fig. 8(a)] and width-10 [Fig. 11(a)]. While the strength of the dimerization, where present, clearly weakens for smaller J', it nevertheless appears to persist for finite $J' < 1$.

A typical symmetry-broken state for the width-6 system is shown in Fig. 9, with a similar pattern arising for the width-10 system. Here, J' was chosen such that the bond strength $\langle S \cdot S \rangle_J$ along the chains just crosses zero [cf. Fig. 8(a)]. Note that a dimerization pattern as in Fig. 9 has been recently also observed on an isotropic four-leg triangular ladder with additional ring exchanges.[32] Overall, the dimerization seen here suggests a qualitative difference of the systems of width $4n + 2$ (symmetry-broken systems), with n an integer, to systems of width $4n$ (uniform systems), while nevertheless, a two-chain periodicity perpendicular to the chains is maintained in either case. Equivalently, this translates into an even-odd effect in the number of laterally coupled zigzag chains. As the dimerization clearly weakens with increasing system width, however, in the thermodynamic limit, the dimerization is
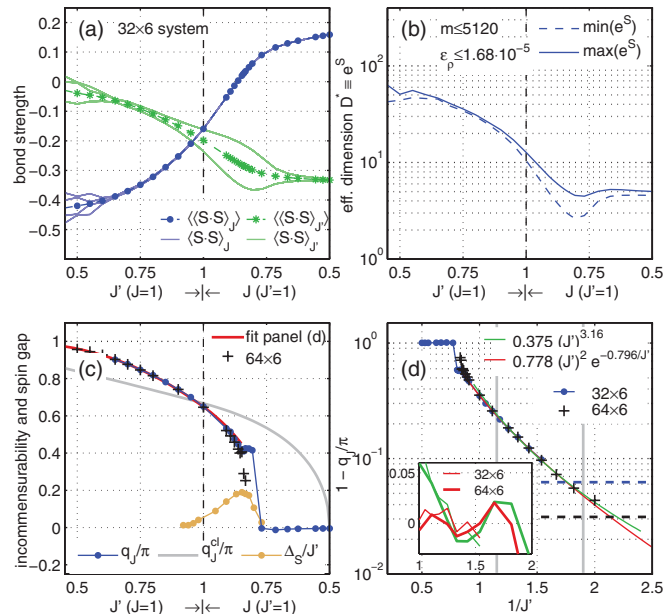
FIG. 8. (Color online) Analysis of 64×6 system using cps-BC (analysis is similar to Fig. 6; for a detailed description of panels, and insets see caption there). The system again shows spontaneous symmetry breaking, with the associated dimerization pattern at $J' = 1.16$ shown in Fig. 9. Strong finite-size and convergence issues are seen for $J' \lesssim 0.6$ in (a) and (b). The phase boundary for incommensurate behavior (panel c) is given by $J' \leqslant J'_c \simeq 1.27$. Similar to the width-2 system, the exponential fit as in Eq. (7) in (d) results in $c_3 \simeq 2$, thus, c_3 has been fixed to this value.

expected to vanish completely, resulting in a consistent picture, independent of the actual system width.

The reoccurrence of the dimerization in the width ($4n + 2$) systems in Figs. 8 and 11 is also reflected in several other quantities, similar to what has already been seen in the width-2 system in Fig. 6. Specifically, in the parameter range where
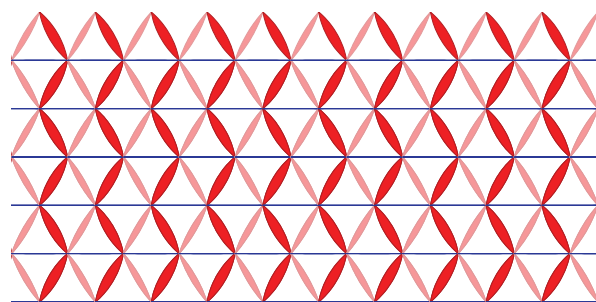

FIG. 9. (Color online) Spontaneously symmetry-broken ground state of the 64×6 system [Fig. 8 at $J' = 1.16$, having $m = 4096$ states kept, with the chain coupling J' chosen such that the intrachain bond strength $\langle S \cdot S \rangle_J$ just crosses zero in Fig. 8(a)]. The figure shows the extremely uniform $\langle S \cdot S \rangle_J$ and $\langle S \cdot S \rangle_{J'}$ across the central region of the system, having $\langle S \cdot S \rangle_{J'} \in \{-0.3453, -0.2039\}$ and $\langle S \cdot S \rangle_J = 0.0038$, with deviations below given accuracy. This underlines the *in*-sensitivity to the open boundaries having cps-BC. With $\langle S \cdot S \rangle_J$ (horizontal bonds) still slightly positive, it is indicated in blue (black) vs. red (gray) for negative values. The weaker interchain bond is shown in lighter color for increased contrast.
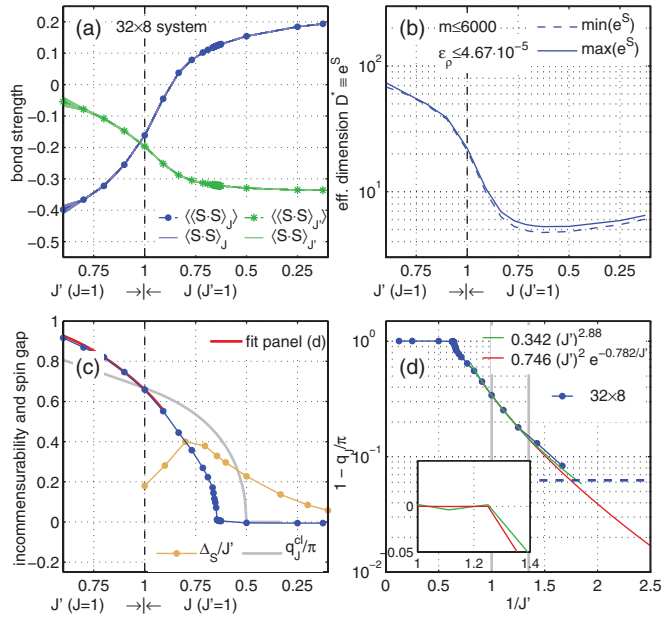
FIG. 10. (Color online) Analysis of 64×8 system using cps-BC (analysis is similar to Fig. 6; for a detailed description of panels and insets, see caption there). The system is uniform without any spontaneous symmetry breaking, with incommensurate behavior for $J' \leqslant J'_c \simeq 1.56$. Finite-size and convergence issues are seen for $J' \lesssim 0.6$ in panel (a), with significant numerical truncation starting with $J' \lesssim 0.8$, as indicated by the artificial suppression (kink) of D^* in panel (b). The exponential fit in panel (d) uses $c_3 = 2$ [cf. Eq. (7)], although the fitting range no longer supports a clear preference for either $c_3 = 1$ or 2.
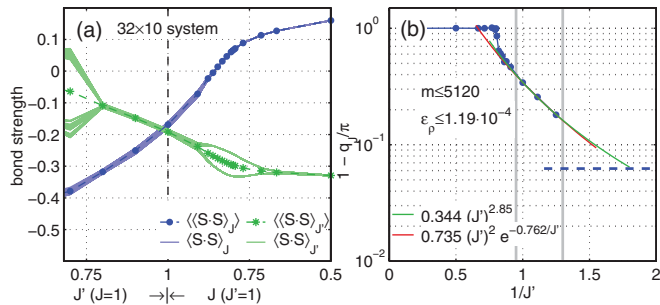

FIG. 11. (Color online) Analysis of $\langle S \cdot S \rangle$ correlations for width-10 system using cps-BC with a similar analysis as in panels (a) and (d) of 6 (for a more detailed description, see caption there). The system again shows spontaneous symmetry breaking in terms of a dimerization bubble for larger J'. The regime $J' \lesssim 0.8$ suffers strong numerical limitations [panel (a)]. Panel (b) analyzes the incommensurate behavior with tentative fits to the regime $J' < 1$ using $c_3 = 2$ [cf. Eq. (7) and other symmetry-broken systems]. The incommensurate phase terminates at $J' \lesssim J'_c \simeq 1.27$. The horizontal dashed line again indicates $2/L$, i.e., the smallest $\tilde{q}_J/\pi \equiv 1 - q_J/\pi$ reachable for given system size. There, however, the block entropy has already grown to such an extent that this limit is no longer reachable reliably numerically.

the dimerization is strongest [e.g., where the lower branch in the $\langle S \cdot S \rangle_{J'}$ bubble reaches a minimum in panels (a)], (i) also a minimum is seen in the effective dimension D^* in panels (b), while (ii) at the same time the incommensurate behavior

terminates in panels (c) [panel (b) of Fig. 11]. For the width-2 system (Fig. 6), this exactly corresponds to the Majumdar-Ghosh point $J' = 2$, while for the width-6 system (Fig. 8) as well as for the width-10 system (Fig. 11) this occurs at $J'_c \simeq 1.27$. Interestingly, in all symmetry-broken cases, the strongest dimerization always occurs around the zero-transition of the bond strength $\langle S \cdot S \rangle_J$ along the chains [compare panels (a)].

In contrast, the non-symmetry-broken width-$4n$ systems show an effectively flat D^* for $J' > 1$, as seen for width-4 in Fig. 7(b) and width-8 in Fig. 10(b). At closer inspection, nevertheless a shallow minimum in D^* is discernible, which within the accuracy of our data again also coincides with the point where the incommensurate behavior terminates. In contrast to the symmetry-broken systems, this typically occurs at a somewhat larger J' still, i.e., at $J'_c \simeq 1.78$ for the width-4 system [Fig. 7(c)] and $J'_c \simeq 1.56$ for the width-8 system [Fig. 10(c)]. The larger J'_c is also reflected in a qualitatively different shape of the curve of the incommensurate wave vector q_J as compared to the symmetry-broken systems.

For the phase boundary where the incommensurate behavior vanishes, a numerical analysis suggests that $q_J(J') \sim |J' - J'_c|^{1/2}$ for $J' \to (J'_c)^-$. This is particularly so for the width-2 system, while for larger widths the incommensurate data is not as reliable to make a definitive statement. The reason being that, at the point where the incommensurate behavior vanishes, typically also the correlation length ξ becomes shortest, e.g., even vanishing for the width-2 system. Consequently, only a very short spatial range is accessible to determine q_J from the S_z data, which for all systems is much shorter than the actual chain length analyzed. While the extraction still works relatively well for width-2 and width-4 systems, the q_J data becomes more noisy for the width-6 system, as seen, for example, in Fig. 8(c) around $J'_c \simeq 1.27$.

Similarly, also the spin gap Δ_S/J' reflects the qualitatively different behavior of the non-symmetry-broken width-$4n$ systems [Figs. 7(c) and 10(c)], in that it saturates for large J' at a finite value. This value, however, appears to diminish rapidly with increasing width. For the symmetry-broken systems of width-2 and width-6, on the other hand, the spin gap vanishes for large J'. Both sets of systems lead us to conclude that the spin gap vanishes in the thermodynamic limit.

2. Small chain couplings

The small J' regime is increasingly affected by finite-size effects and limited numerical resources for the wider systems, where the entanglement across the chains increases strongly. This limits the numerically accessible range. For the width-4 system in Fig. 7, for $J' \lesssim 0.5$, a slight spread is seen in the individual bond correlations (solid lines) in Fig. 7(a), and more pronouncedly, in Fig. 7(b) where the effective dimension D^* is cut off by the maximum number of states that could be kept ($m \leqslant 7000$). Similar to the width-2 system, D^* shows a strong exponential increase for intermediate decreasing $J' < J'_c \simeq 1.78$. For the width-6 system, strong convergence issues arise for $J' \lesssim 0.6$ [Fig. 8(a)], for the width-8 system for $J' \lesssim 0.7$ [Fig. 10(a)], and for the width-10 system for $J' \lesssim 0.8$ [Fig. 11(a)]. In the latter case, the accuracy is already also compromised for intermediate J', as seen by the slight spread in the individual bond data for $J' \lesssim 1.10$.
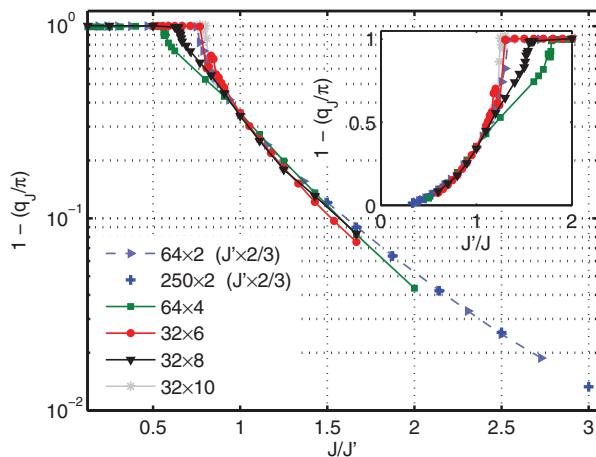
FIG. 12. (Color online) Summarized incommensurate data $\tilde{q}_J \equiv \pi - q_J$ for width-2 to width-10 systems [Figs. 6–10, panel (d), and Fig. 11(b), respectively]. For wider systems, the incommensurate phase terminates at $J_c' \simeq 1.25$. The inset shows the same data vs. J' on a linear scale.
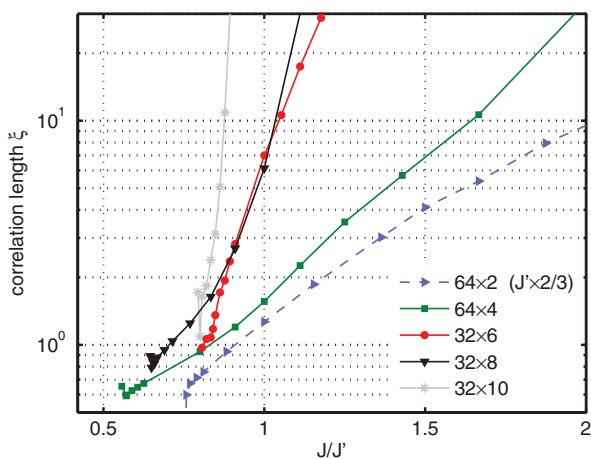

FIG. 13. (Color online) Combined data of correlation length defined through Eq. (5) for width-2 to width-10 systems. The correlation length is shown only in the parameter regime where the systems show incommensurate behavior. Outside this range (i.e., for large J'/J), depending on system width, exponential decay can be replaced by algebraic decay.

Bearing in mind this limited numerical accessibility of small J', the incommensurate behavior for smaller J' is analyzed exactly the same way as for the width-2 system in Fig. 6(d) for the width-4 [Fig. 7(d)], width-6 [Fig. 8(d)], width-8 [Fig. 10(d)], and the width-10 system [Fig. 11(b)]. The data was fitted both with an exponential fit as in Eq. (7), as well as with a plain polynomial fit. Interestingly, for all systems from width-2 to width-10, the plain polynomial fit $q_J \sim (J')^3$ does represent a very close fit, in agreement with Ref. 14. However, similar to the discussion of the width-2 system, there appear systematic deviations that can be improved upon by using an exponential fit. This is clearly seen for the width-4 system [see inset to Fig. 7(d)], and to a somewhat lesser degree given numerical limitations for the width-6 [Fig. 8(d)] or width-8 system [Fig. 10(d)].

Finally, the incommensurate data of all systems analyzed [Figs. 6–10, panel (d), and Fig. 11(b)] is summarized in Fig. 12. Since the data for the width-2 system is calculated without periodic wrapping (as this just doubles the strength of the interactions of *existing* bonds between the chains), a factor of 2/3 was applied onto J' for the width-2 system such that the incommensurate data visibly coincides at $J' = 1$ with the data from the wider systems. With this, for smaller J' (large J/J'), the incommensurate data shows little qualitative and quantitative differences. This supports the intuitive notion that, as the chains become more and more independent, the dependence of the incommensurate behavior on the actual system width also weakens. In particular, none of the data indicates that the incommensurability may vanish for small but finite J'.

3. Correlation length

In contrast to the incommensurate wave vectors, the correlation length ξ still shows a pronounced dependence on the system width. Following the analysis in Eq. (5), in the incommensurate regime aside from the oscillating behavior that determines q_J, a clear exponential decay is observed and fitted in the central area of the system away from the open left and right boundaries (cf. Figs. 4 and 5). The combined results for width-2 to width-10 are shown in Fig. 13. The horizontal axis of the width-2 system again has been scaled the same way as shown and discussed with Fig. 12. Considering the qualitative difference between width-$4n$ and width-$(4n + 2)$ systems then, only width-(2, 6, 10,...) or width-(4, 8,...) may be directly comparable. This strongly limits finite-size analysis in terms of the system width. While the correlation length strongly grows with the width of the systems, consistent with the fact, for example, that the isotropic case has finite magnetization,[16] nevertheless, finite-size scaling in the width of the system would be crucial in the explicit determination of the existence of magnetization for arbitrary J' in the thermodynamic limit. This is thus beyond the scope of this paper.

IV. SUMMARY AND OUTLOOK

The incommensurate correlations on the anisotropic spin-1/2 Heisenberg lattice have been analyzed over a wide range of chain couplings J'/J. The incommensurate behavior in terms of the Brillouin zone of a single chain is found to change smoothly from $q_J \to \pi$ for weak chain coupling to $q_J = 0$ for $J' \geqslant J_c' > 1$. In particular, our results are consistent with the 120° order for the isotropic lattice, which is also reflected in the crossing of q_J with the classical incommensurability q_J^{cl} at $J' = 1$ in panel (c) of Figs. 7–10. Away from the isotropic point, the 120° order in the spin correlations changes *smoothly* into the 1D-AF correlations for $J' < 1$ or into the square AF correlations for $J' \geqslant J_c'$. Note that the emphasis here is on the relative order of *spin correlations*, rather than on explicit magnetization.[16] The latter is out of the scope of this paper and thus left as an outlook.

Given the strong frustration in the system, one may expect that for smaller interchain couplings J' the actual data becomes less sensitive to the width of the system [14] (see Fig. 12). Therefore, already the narrower even-width

systems provide a good qualitative description of the two-dimensional triangular lattice in the regime of small J'. Finite-size effects on our cylinders include symmetry-broken and non-symmetry-broken ground states as for width-$(4n + 2)$ and width-$4n$ systems, respectively, so extrapolations in the width should separate these two classes.[10,14] From the analysis of the incommensurate data, we find that exponential fits of the form Eq. (7) fit the data for the incommensurate wave vectors best. While the accessible range is limited to finite J', we nevertheless see very systematic behavior for smaller J' down to $J' \gtrsim 0.5$ where the correlations between the chains are already strongly reduced due to inherent frustration. We take this as indication that the exponential behavior is valid down to $J' = 0$. That is, the incommensurate behavior remains present for any finite $0 < J' < J'_c$. Given the derived exponential fits, one may estimate the required system sizes for $J' < 0.5$. Taking $J' = 0.2$ for the width-4 (width-6) system, for example, a system length of $\gtrsim 8700$ sites ($\gtrsim 3400$ sites) would be required, respectively. From a DMRG point of view, this is completely out of reach at this stage. It needs to be seen to what extent recently emerging infinite-size algorithms, such as iTEBD[33] or iDMRG,[34] will be able to deal with this kind of situation while bearing in mind that incommensurate correlations with an (exponentially) large underlying wavelength represent a delicate issue.

Meanwhile, experimental quantum simulations utilizing ultracold atoms are making rapid progress. With simulations on the classical anisotropic Heisenberg lattice performed successfully recently,[35] this provides the exciting outlook that the simulation of quantum spin models may become accessible to this highly controlled experimental arena in the near future.

[1] R. Coldea, D. A. Tennant, K. Habicht, P. Smeibidl, C. Wolters, and Z. Tylczynski, Phys. Rev. Lett. **88**, 137203 (2002).

[2] O. A. Starykh, H. Katsura, and L. Balents, Phys. Rev. B **82**, 014421 (2010).

[3] Y. Shimizu, K. Miyagawa, K. Kanoda, M. Maesato, and G. Saito, Phys. Rev. Lett. **91**, 107001 (2003).

[4] H. C. Kandpal, I. Opahle, Y.-Z. Zhang, H. O. Jeschke, and R. Valentí, Phys. Rev. Lett. **103**, 067004 (2009).

[5] Y. Qi, C. Xu, and S. Sachdev, Phys. Rev. Lett. **102**, 176401 (2009).

[6] L. Balents, Nature (London) **464**, 199 (2010).

[7] Zheng Weihong, R. H. McKenzie, and R. R. P. Singh, Phys. Rev. B **59**, 14367 (1999).

[8] M. Bocquet, F. H. L. Essler, A. M. Tsvelik, and A. O. Gogolin, Phys. Rev. B **64**, 094425 (2001).

[9] M. Q. Weng, D. N. Sheng, Z. Y. Weng, and R. J. Bursill, Phys. Rev. B **74**, 012407 (2006).

[10] O. A. Starykh and L. Balents, Phys. Rev. Lett. **98**, 077205 (2007).

[11] D. Heidarian, S. Sorella, and F. Becca, Phys. Rev. B **80**, 012404 (2009).

[12] J. Reuther and R. Thomale, Phys. Rev. B **83**, 024402 (2011).

[13] P. Hauke, T. Roscilde, V. Murg, J. I. Cirac, and R. Schmied, New J. Phys. **13**, 075017 (2011).

[14] S. Ghamari, C. Kallin, S.-S. Lee, and E. S. Sørensen, Phys. Rev. B **84**, 174415 (2011).

[15] S. R. White, Phys. Rev. Lett. **69**, 2863 (1992).

[16] S. R. White and A. L. Chernyshev, Phys. Rev. Lett. **99**, 127004 (2007).

[17] S. Yan, D. A. Huse, and S. R. White, Science **332**, 1173 (2011).

[18] E. M. Stoudenmire and S. R. White, e-print arXiv:1105.1374v2 [cond-mat.str-el].

[19] M. Bode, M. Heide, K. von Bergmann, P. Ferriani, S. Heinze, G. Bihlmayer, A. Kubetzka, O. Pietzsch, S. Blugel, and R. Wiesendanger, Nature (London) **447**, 190 (2007).

[20] C. Griset, S. Head, J. Alicea, and O. A. Starykh, e-print arXiv:1107.0772v4 [cond-mat.str-el].

[21] A. Yoshimori, J. Phys. Soc. Jpn. **14**, 807 (1959).

[22] J. Merino, R. H. McKenzie, J. B. Marston, and C. H. Chung, J. Phys.: Condens. Matter **11**, 2965 (1999).

[23] S. R. White and I. Affleck, Phys. Rev. B **54**, 9862 (1996).

[24] S. Rommer and S. Östlund, Phys. Rev. B **55**, 2164 (1997).

[25] U. Schollwöck, Ann. Phys. (NY) **326**, 96 (2011).

[26] G. Misguich, C. Lhuillier, B. Bernu, and C. Waldtmann, Phys. Rev. B **60**, 1064 (1999).

[27] M. Vekić and S. R. White, Phys. Rev. Lett. **71**, 4283 (1993).

[28] M. J. de Oliveira, Phys. Rev. B **48**, 6141 (1993).

[29] S. Eggert, Phys. Rev. B **54**, R9612 (1996).

[30] C. K. Majumdar and D. K. Ghosh, J. Math. Phys. **10**, 1388 (1969).

[31] D. N. Aristov, C. Brünger, F. F. Assaad, M. N. Kiselev, A. Weichselbaum, S. Capponi, and F. Alet, Phys. Rev. B **82**, 174410 (2010).

[32] M. S. Block, D. N. Sheng, O. I. Motrunich, and M. P. A. Fisher, Phys. Rev. Lett. **106**, 157202 (2011).

[33] G. Vidal, Phys. Rev. Lett. **98**, 070201 (2007).

[34] I. P. McCulloch, e-print arXiv:0804.2509v1 [cond-mat.str-el].

[35] J. Struck, C. Ölschläger, R. Le Targat, P. Soltan-Panahi, A. Eckardt, M. Lewenstein, P. Windpassinger, and K. Sengstock, Science **333**, 996 (2011).